1

Supplemental Information

3

Subtle tuning of nanodefects actuates highly efficient electrocatalytic oxidation

6

Yifan Gao[a, 1], Shuai Liang[b, 1*], Biming Liu[a], Chengxu Jiang[a], Chenyang Xu[a], Xiaoyuan Zhang[a], Peng Liang[a], Menachem Elimelech[c*], Xia Huang[a*]

9

[a]State Key Joint Laboratory of Environment Simulation and Pollution Control, School of Environment, Tsinghua University, Beijing 100084, China

[b]Beijing Key Lab for Source Control Technology of Water Pollution, College of Environmental Science and Engineering, Beijing Forestry University, Beijing 100083, China

[c]Department of Chemical and Environmental Engineering, Yale University, New Haven, CT 06520-8286, USA

16

*Corresponding author: E-mail: xhuang@tsinghua.edu.cn;

*Corresponding author: E-mail: shuai_liang@bjfu.edu.cn
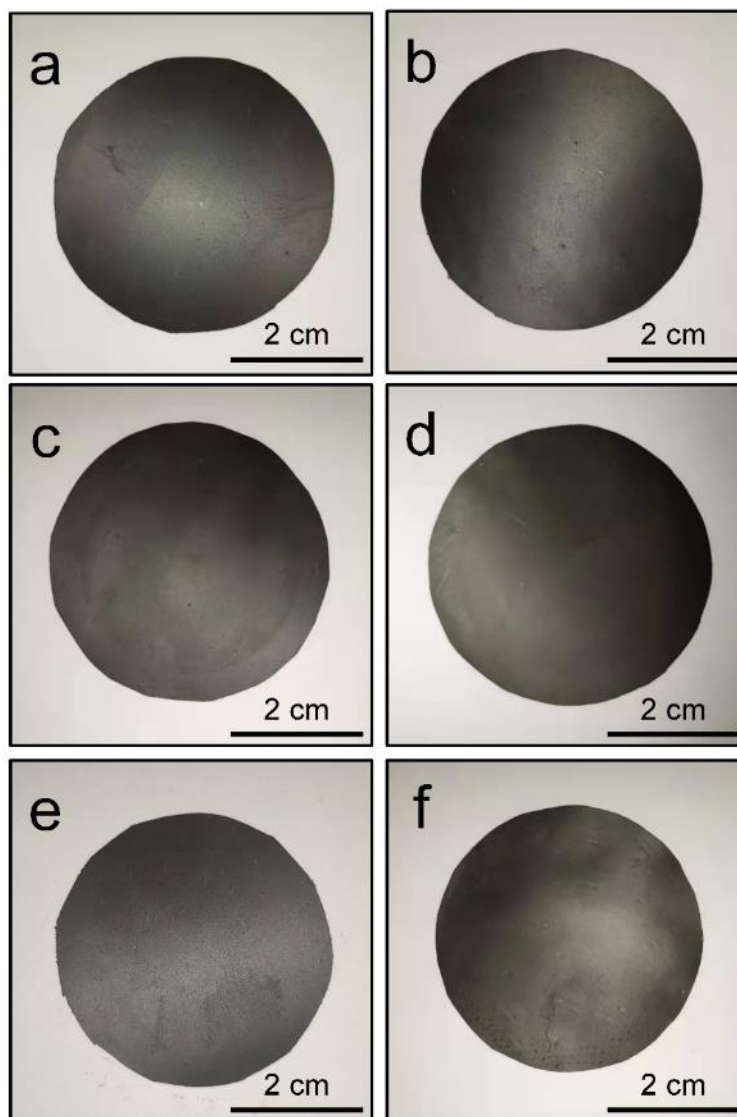
*Corresponding author: E-mail: meachem.elimelech@yale.edu

[1]Y.G. and S.L. contributed equally to this work
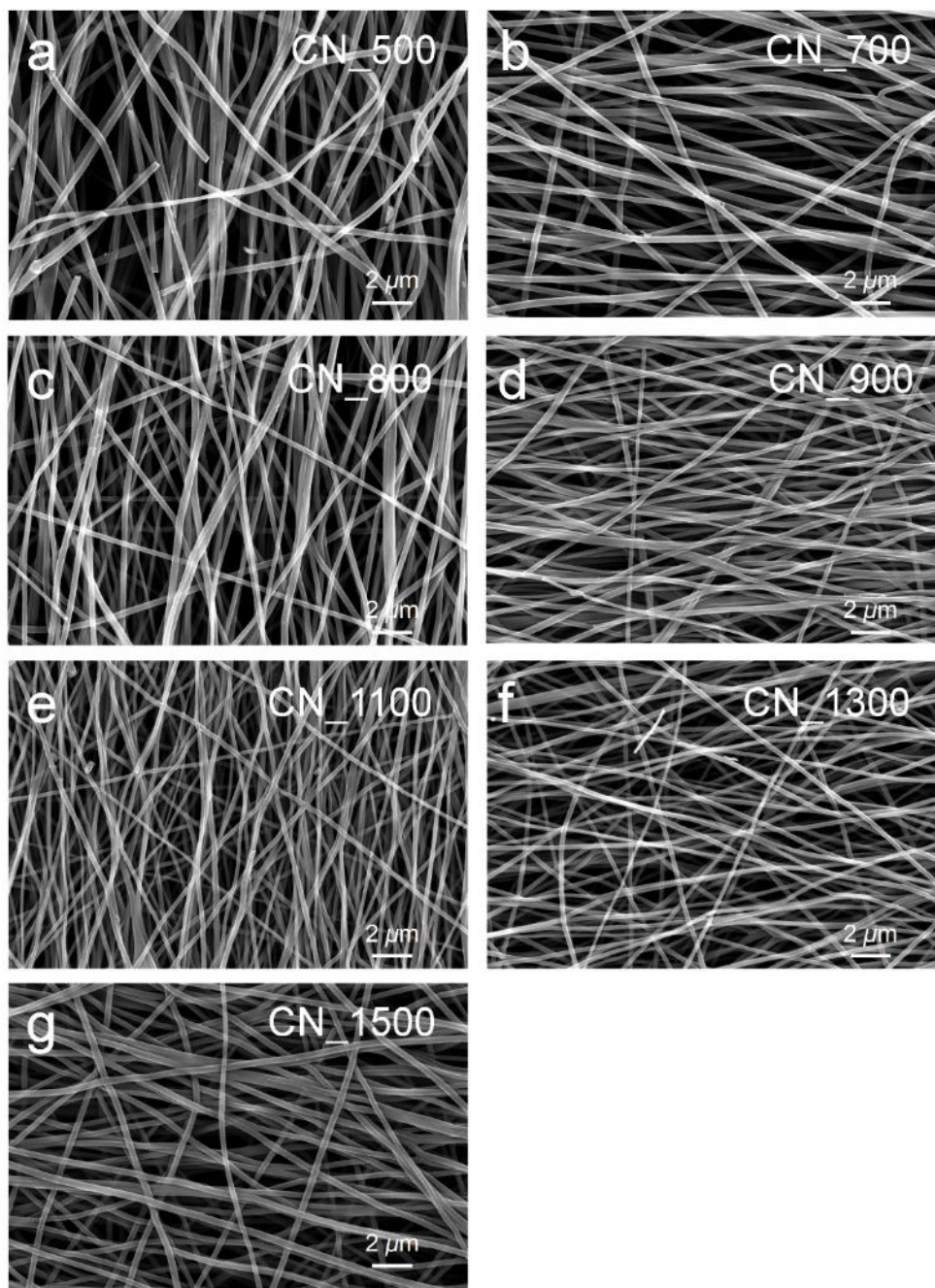
21

This PDF file includes:
 Supplementary Note 1 to 3
 Supplementary Figures 1 to 29
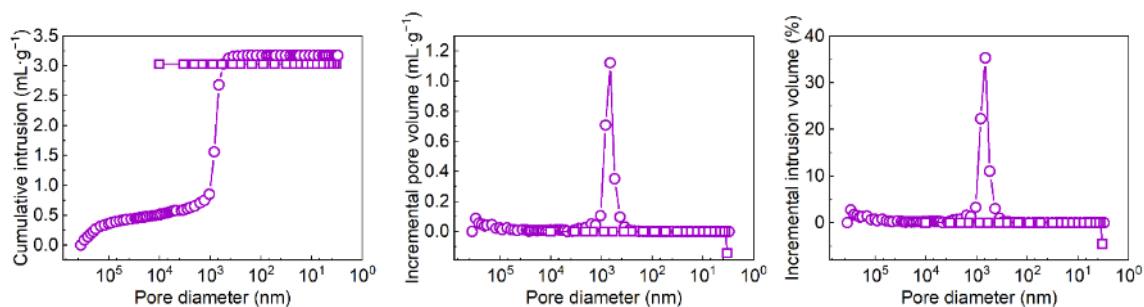 Supplementary Tables 1 to 5

26

Supplementary Figure 1. Photographs of the different CN membranes (i.e., (**a**) CN_500, (**b**) CN_700, (**c**) CN_800, (**d**) CN_1100, (**e**) CN_1300, and (**f**) CN_1500).

29

Supplementary Figure 2. SEM images of the (**a**) CN_500, (**b**) CN_700, (**c**) CN_800, (**d**) CN_900, (**e**) CN_1100, (**f**) CN_1300, and (**g**) CN_1500 membranes.

Supplementary Figure 3. Results of the mercury intrusion porosimetry method for the prepared CN_900 membrane.
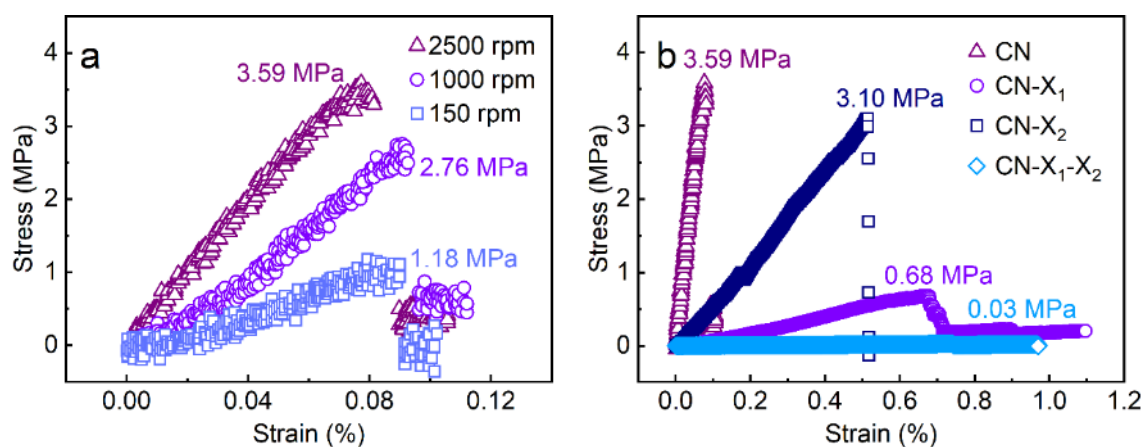
Supplementary Figure 4. Measured tensile stress–strain curves of different CN membranes prepared with (**a**) different cylinder rotation speed and (**b**) different external pressure conditions; the suffixes X_1 and X_2 indicate the absence of the pre-oxidation pressure and the absence of the carbonization pressure, respectively. Note: all the CN membranes in this figure was carbonized at 900 °C.
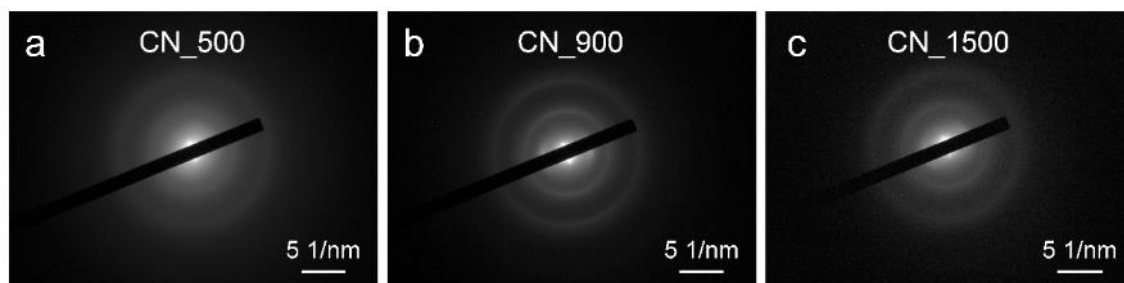
Supplementary Figure 5. Selected area electron diffraction (SAED) patterns of the (**a**) CN_500, (**b**) CN_900, and (**c**) CN_1500.
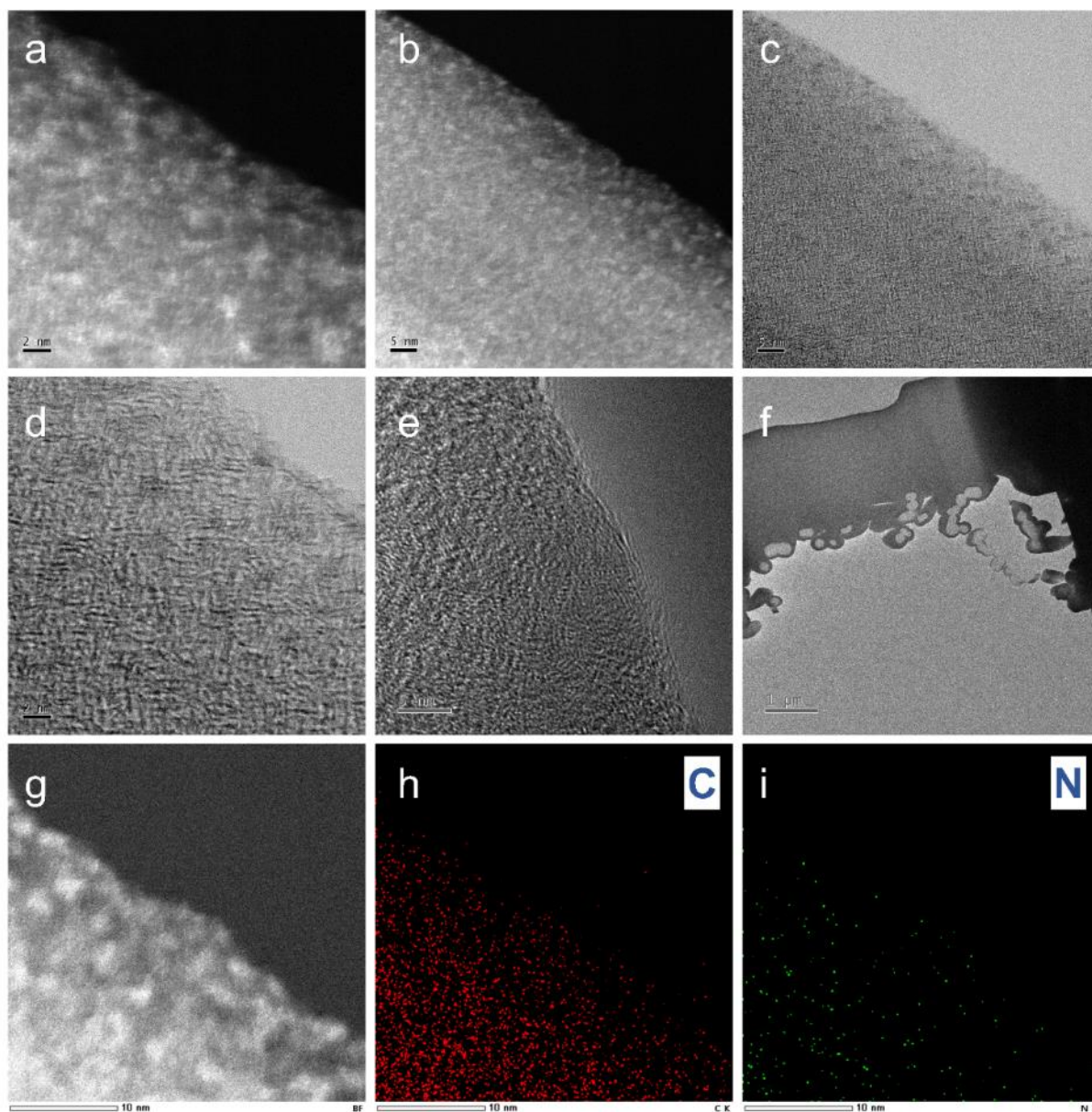
Supplementary Figure 6. (**a** and **b**) High-angle annular dark-field scanning transmission electron microscopy (HAADF-STEM) images of CN_900. (**c** and **d**) Annular bright field scanning transmission electron microscopy (ABF-STEM) images of CN_900. (**e**) HRTEM image of CN_900. (**f**) TEM image showing the CN_900 prepared by focused ion beam-scanning electron microscope (FIB-SEM) technique. (**g**–**i**) Elemental mapping images by EDS of CN_900.

53 **Supplementary Note 1.**

54 The "river like" disturbed lattice structures could hardly be observed in CN_500 (**Figure 2j**),

55 indicating that the graphitization of CN_500 was negligible. As for CN_1500, there were more

56 obvious and longer lattice stripes (**Figure 2l**) with rare amorphous structures. This suggested

57 that the graphitization degree of CN_1500 was the highest, leaving few defective structures.

58
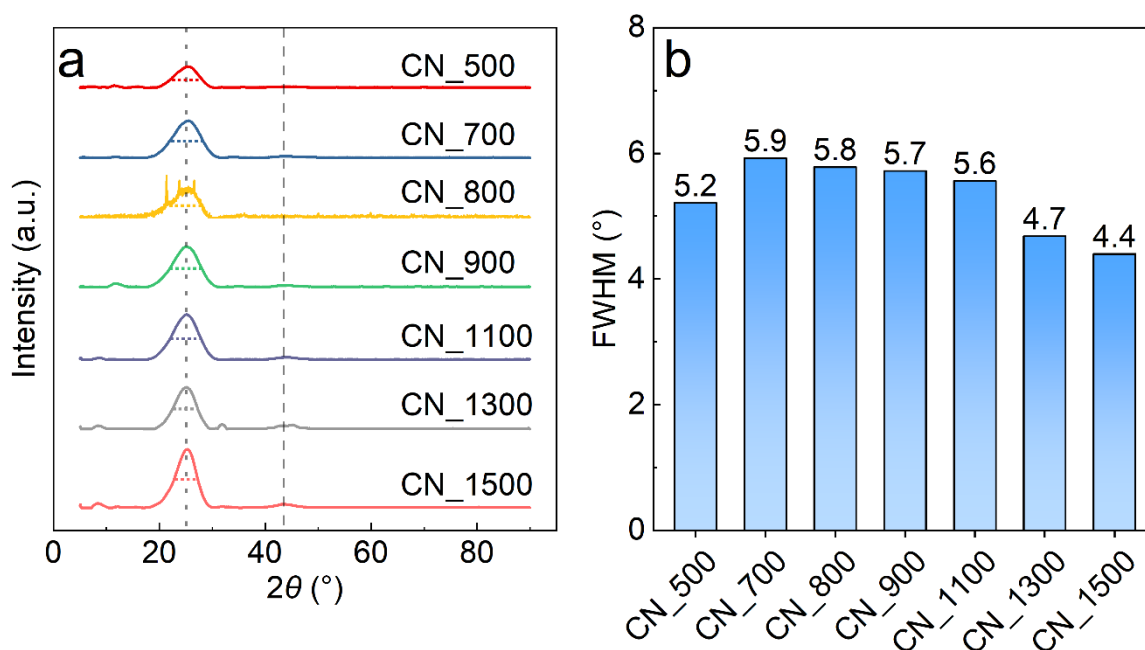
59

60 **Supplementary Figure 7.** (**a**) XRD patterns and (**b**) determined full width at half maximum

61 (FWHM) data of the CN_500, CN_700, CN_800, CN_900, CN_1100, CN_1300, and

62 CN_1500.
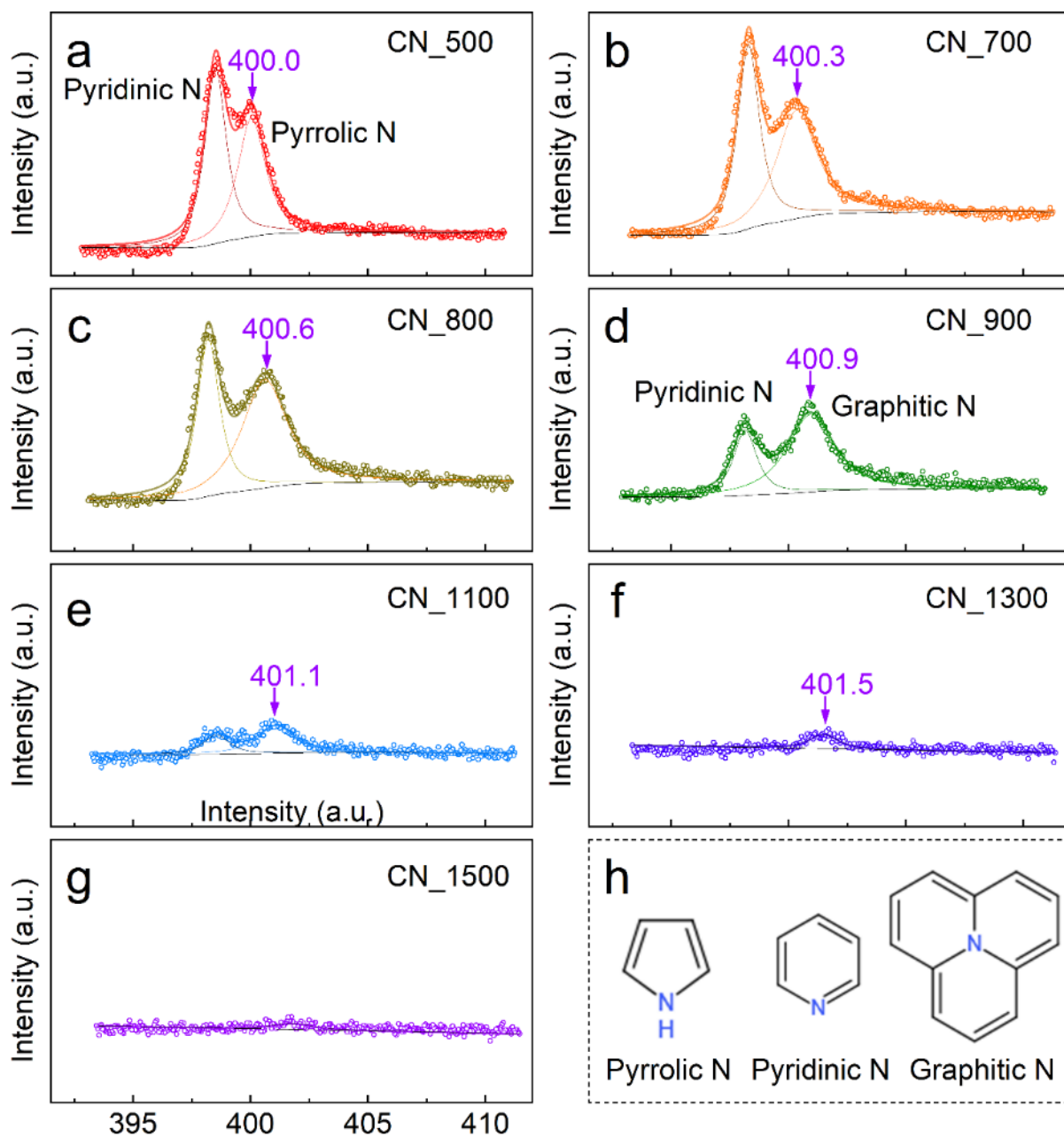
Supplementary Figure 8. High-resolution *N 1s* XPS spectra and fitted curves of the (**a**) CN_500, (**b**) CN_700, (**c**) CN_800, (**d**) CN_900, (**e**) CN_1100, (**f**) CN_1300, and (**g**) CN_1500; and (**h**) chemical structures of pyrrolic N, pyridinic N, and graphitic N.

67
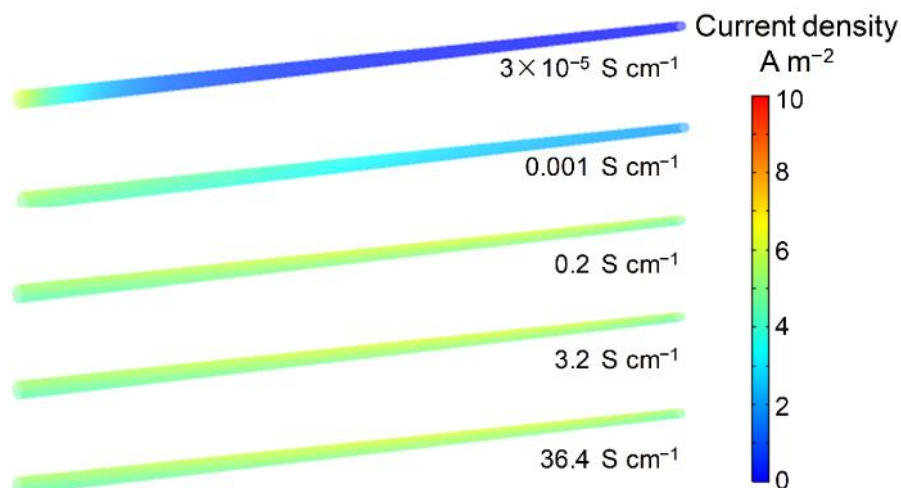
Supplementary Figure 9. Computed distributions of current density (A m^{-2}) on the CN models in different simulation scenarios (**Figure 5**, i.e., at different CN conductivities: 3×10^{-5}, 0.001, 0.2, 3.2, and 36.4 S cm^{-1}).

Supplementary Note 2

The analysis based on Fukui function was used to verify the region of active sites[1] of CNs as well as to predict electrophilic, nucleophilic, and free radical attacks in pollutant regions[2]. The program Multiwfn[3,4] was used to calculate the Fukui function with Hirshfeld charges. As shown in **Supplementary Fig. 10**, the results of the Fukui function analysis of different CNs are similar to the previous DFT calculations results. The f$^-$ distribution of CN_900 was much more inhomogeneous. The regions around the defects have larger values of f$^-$ (**Supplementary Table 1**), which means that these regions are more reactive. The electrophilicity indices of CN_500, CN_900, and CN_1500 unit-regions were calculated to be 1.72, 2.84, and 2.49 eV, respectively. Overall, CN_900 was expected to achieve the highest electrocatalytic reactivity based on the Fukui function analysis. In addition, the Fukui function analysis (**Supplementary Fig. 11** and **Supplementary Table 2**) shows that the amino group (N4) in the PRO structure are more susceptible to electrophilic attack (higher f$^-$) and the benzene ring (C10–13, C15–18) is highly susceptible to free radical attack (higher f^0).

86
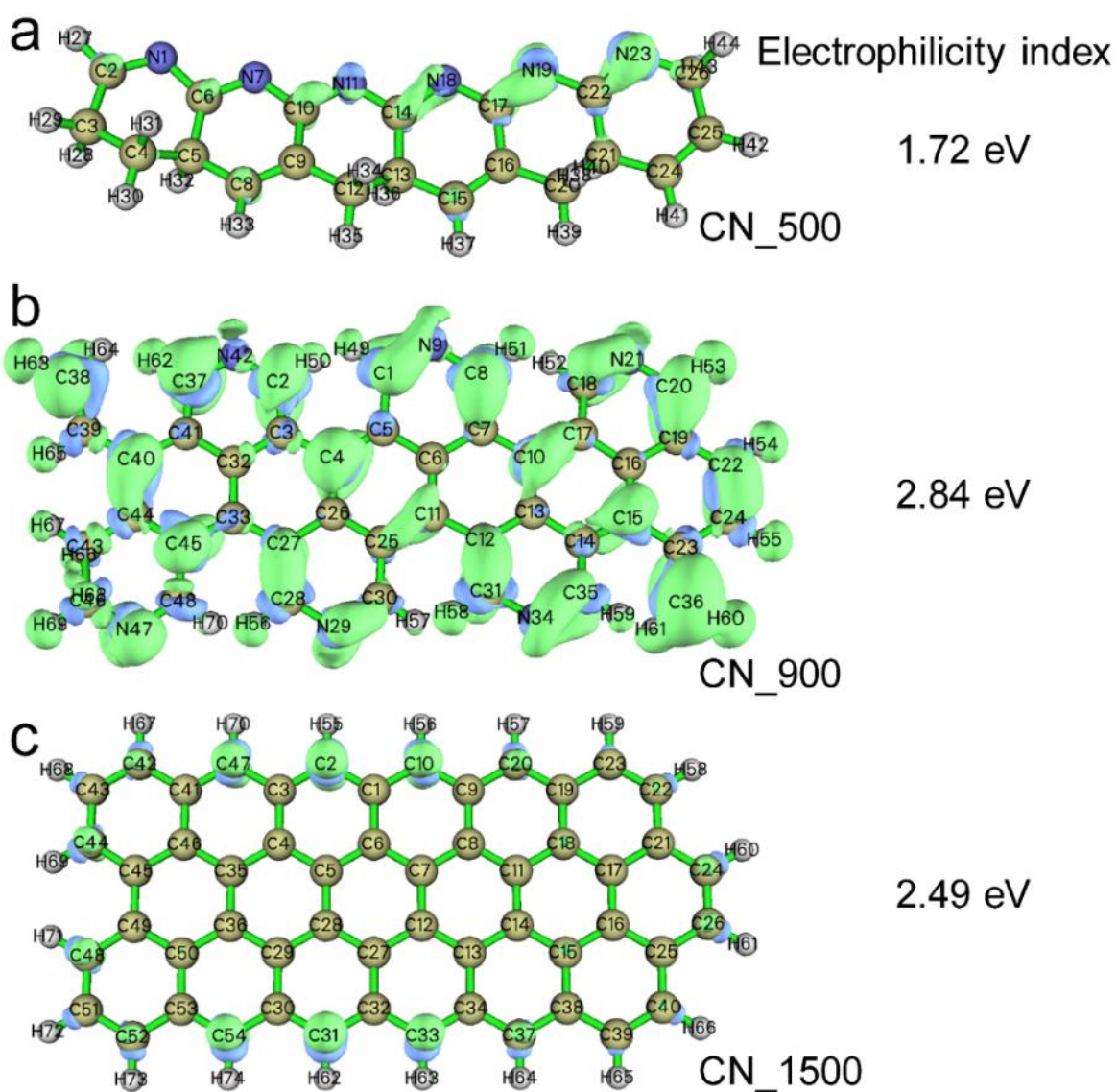
Supplementary Figure 10. Representation of the Fukui function f⁻ of the (a) CN_500, (b) CN_900, and (c) CN_1500. The calculated electrophilicity indices were included.

89
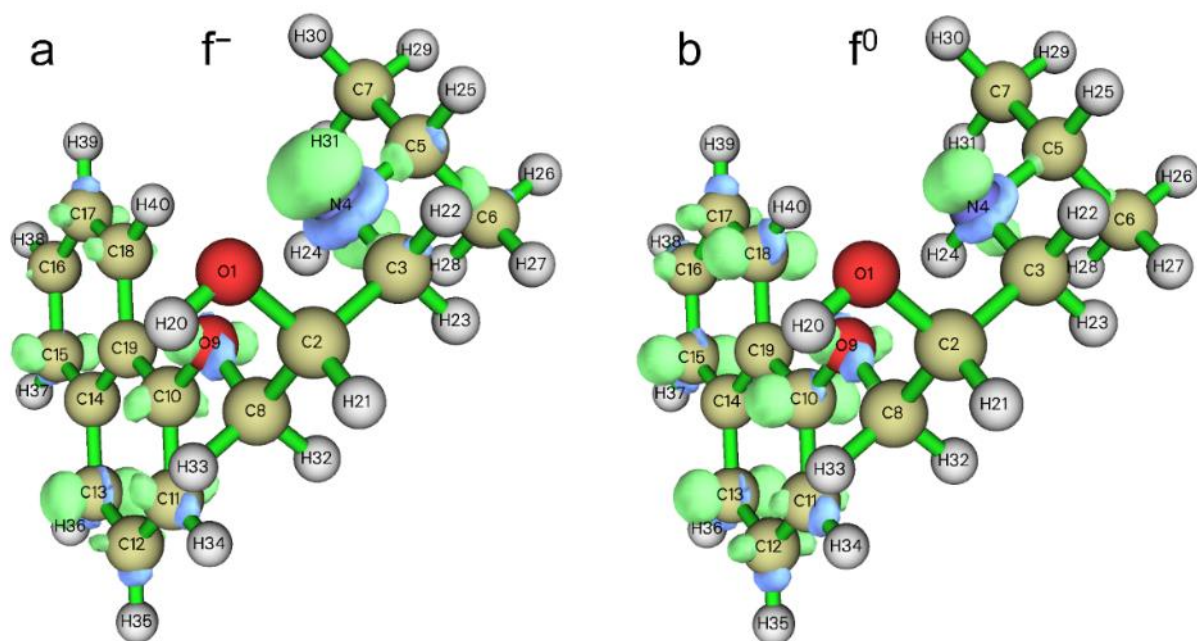
Supplementary Figure 11. Representation of the (a) Fukui function f⁻ and (b) Fukui function f⁰ of the PRO.

92

93
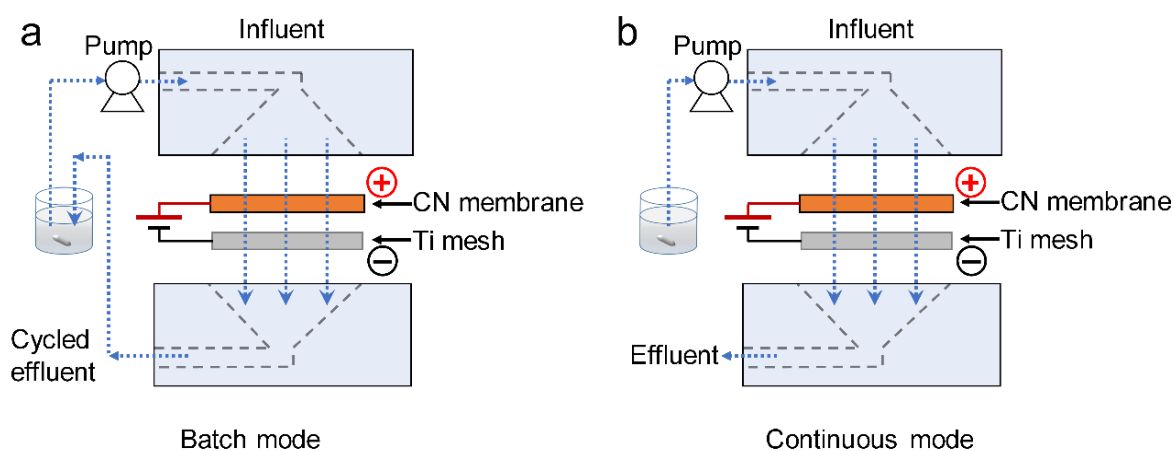
Supplementary Figure 12. Configurations of the electrocatalytic membrane filtration (EMF) system operated at the (**a**) batch mode (i.e., effluent cycles back to feed reservoir, from where the samples are taken for analyses) and (**b**) continuous mode (i.e., feed solution flows one time through the reactor without circulation and the effluent is collected for analyses).

98
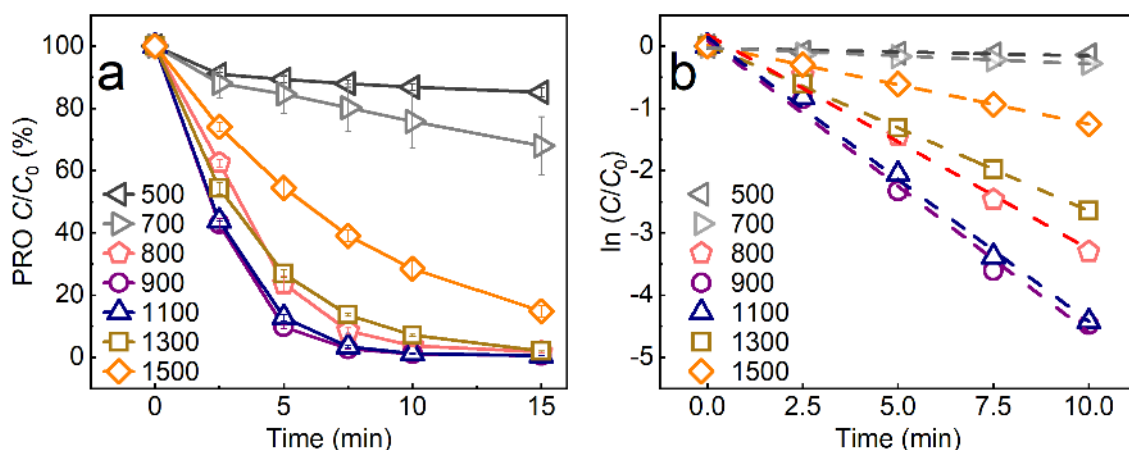
Supplementary Figure 13. Comparison of the electrocatalytic performance in a batch-mode EMF system among the different CN membranes (i.e., CN_500, CN_700, CN_800, CN_900, CN_1100, CN_1300, and CN_1500) in terms of the (a) C/C_0 and (b) $\ln(C/C_0)$ decline trends. The error bars represent the standard deviation and were calculated on the basis of at least three experimental data points.
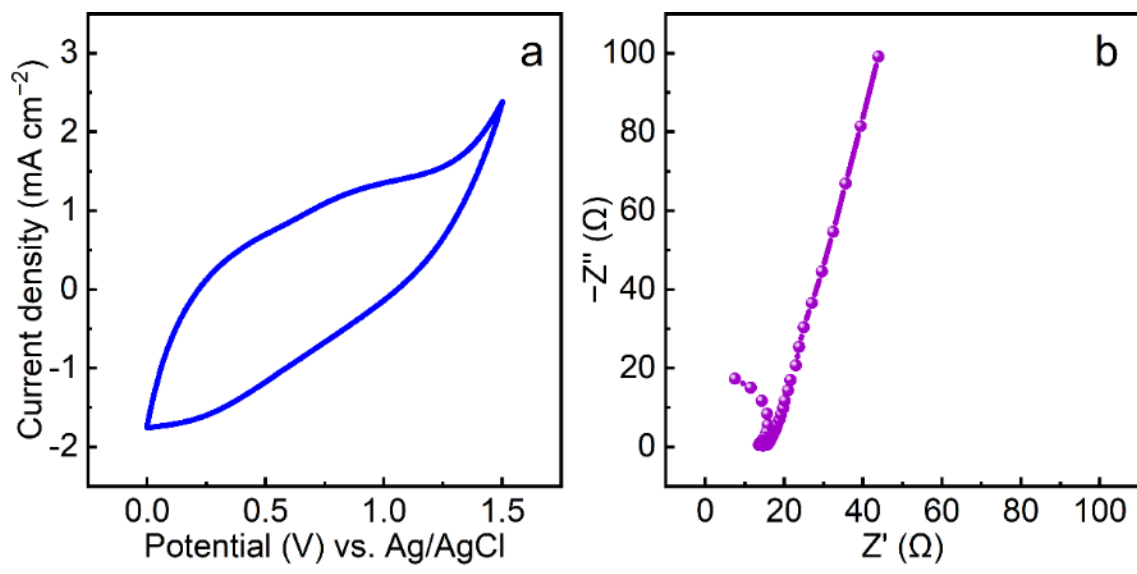
Supplementary Figure 14. (a) Cyclic voltammogram and (b) electrochemical impedance spectroscopy of the CN_900 membrane.
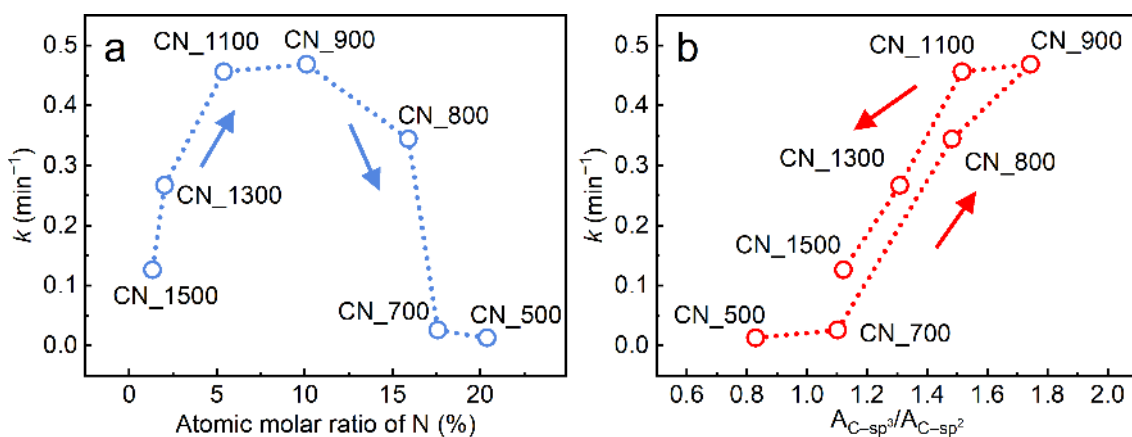
Supplementary Figure 15. (**a**) Correlation analysis between the calculated kinetic constants (k, min^{-1}) of PRO degradation in a batch mode and atomic molar ratios of N for the different CN membranes (i.e., CN_500, CN_700, CN_800, CN_900, CN_1100, CN_1300, and CN_1500). (**b**) Correlation analysis between k (min^{-1}) and A_{C-sp3}/A_{C-sp2} ratio for the different CN membranes.
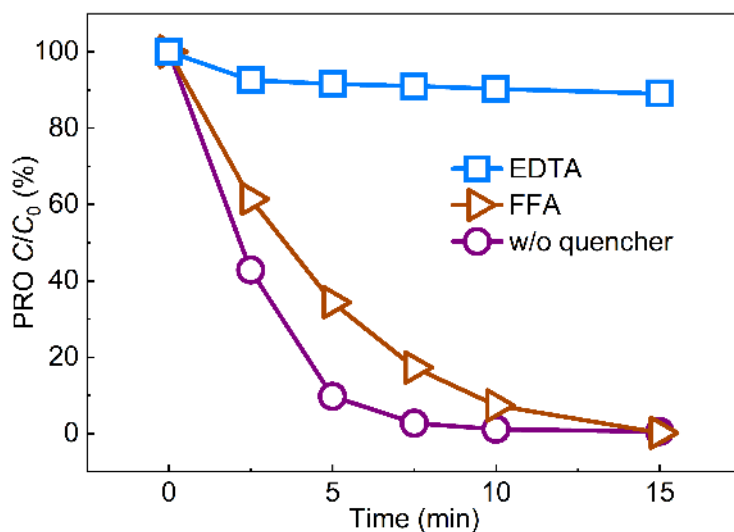
Supplementary Figure 16. Quenching tests revealing the contribution of direct oxidative hole (h$^+$, quenched by 4 mM EDTA-2Na) and singlet oxygen ($^1O_2$, quenched by 16 mM FFA) to the degradation of PRO (20 mg L^{-1}) by the CN_900 membrane.
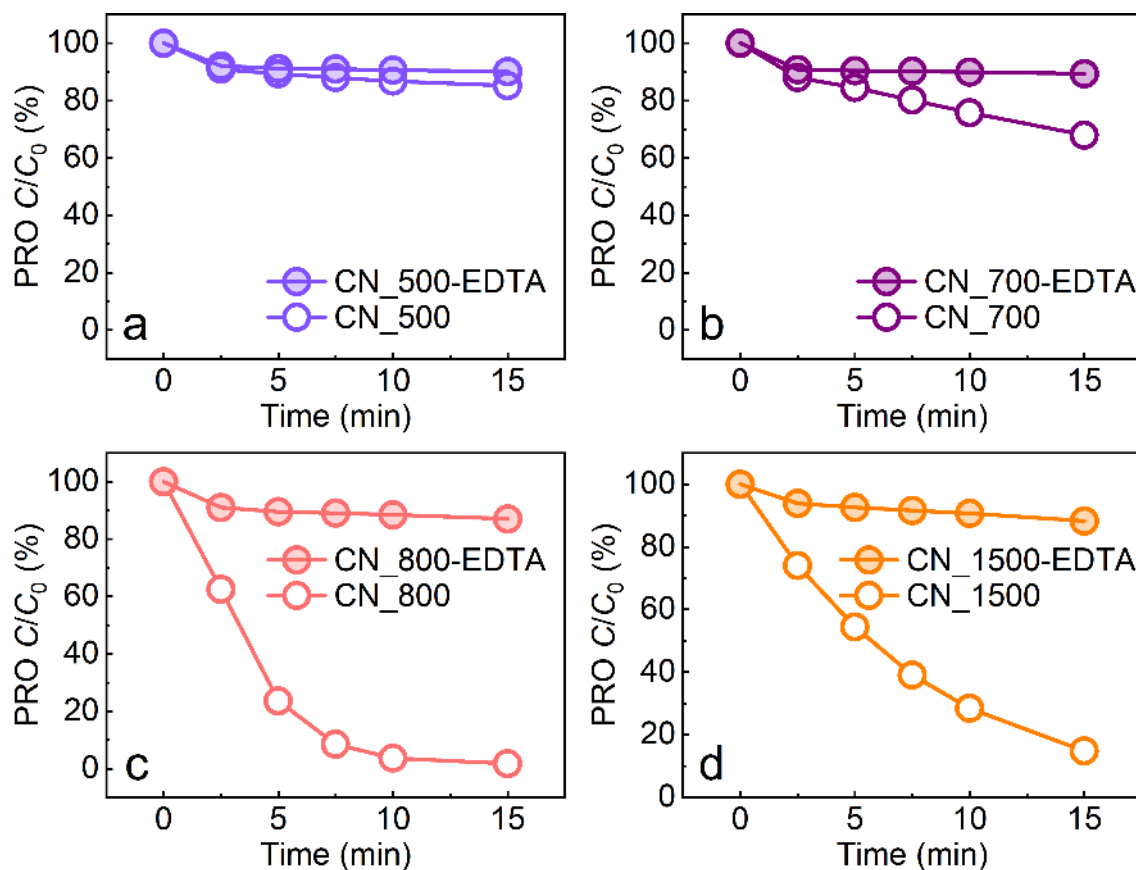
Supplementary Figure 17. Quenching tests revealing the contribution of direct oxidative hole (h^+, quenched by 4 mM EDTA-2Na) to the degradation of PRO (20 mg L^{-1}) for different CN membranes: (**a**) CN_500, (**b**) CN_700, (**c**) CN_800, and (**d**) CN_1500.
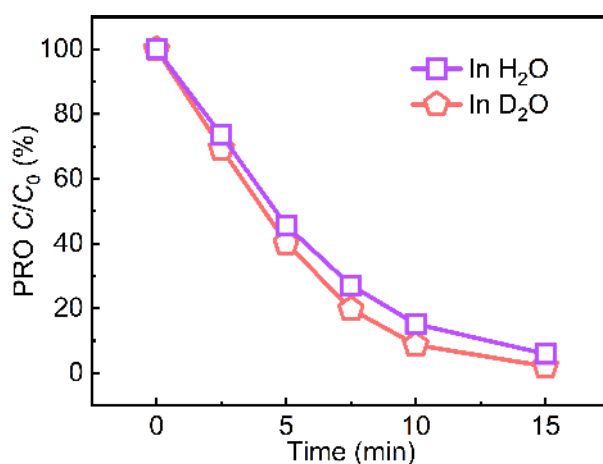
Supplementary Figure 18. Comparison of PRO (50 mg L^{-1}) degradation by CN_900 electrocatalytic membrane in H_2O and D_2O solvents.

129
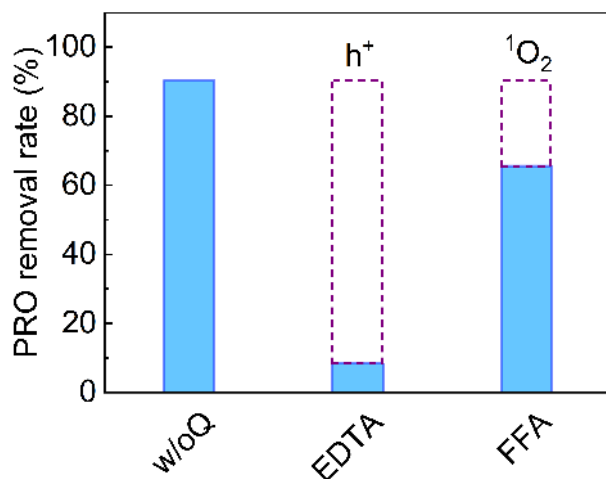
Supplementary Figure 19. Comparison of the PRO removal rates among different EMF tests without the quencher (denoted as w/oQ) or with different quencher (EDTA-2Na and FFA). The reduced portions marked with the dotted boxes indicate the amounts degraded by the quenched oxidants, thus revealing the contribution ratios of different oxidants to pollutant degradation.

134

135
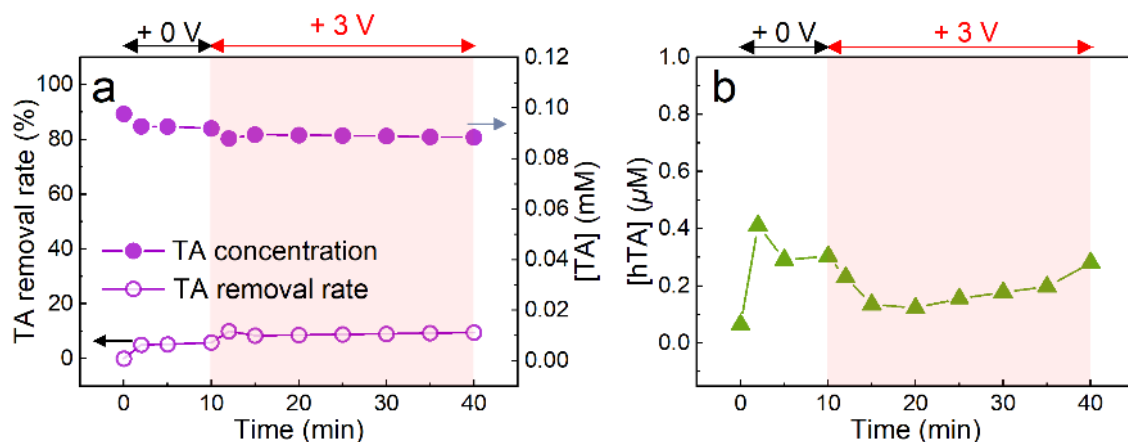
Supplementary Figure 20. Further revealing the mechanism of electrocatalytic degradation performance of the CN_900 membrane. (**a**) Probe test exploring the presence of ·OH through the degradation of 100 μM TA by the CN_900 membrane. (**b**) Variation of the measured concentration of hTA during the probe-test with TA for the CN_900 membrane.

140
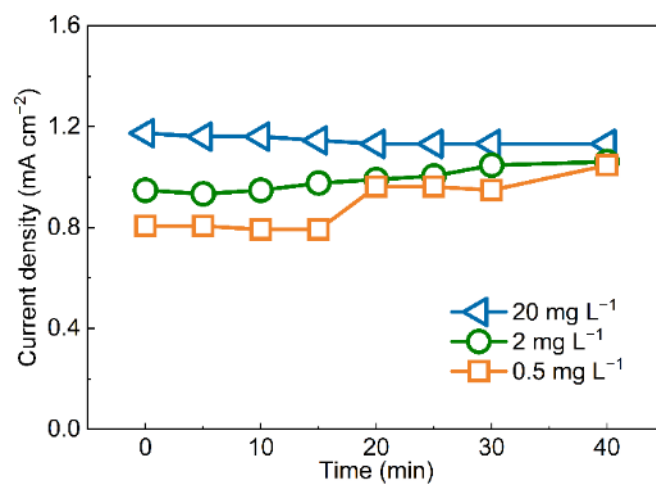
Supplementary Figure 21. Measured current densities (mA cm^{-2}) during the continuous EMF tests with the CN_900 membrane at different PRO concentrations (initial concentration: 20, 2, and 0.5 mg L^{-1}).

144
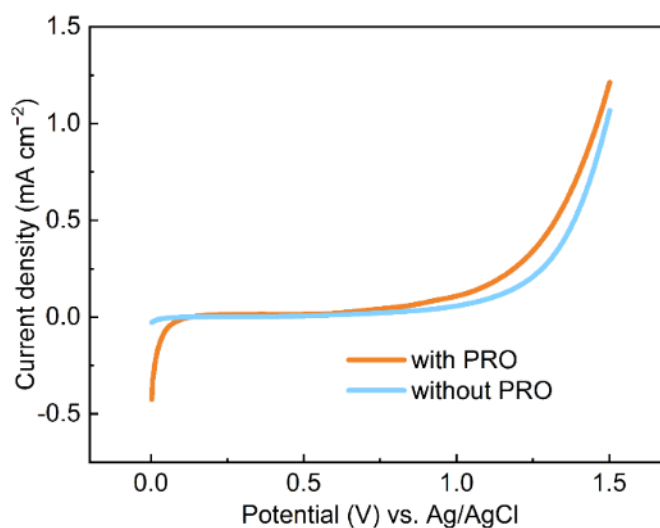
Supplementary Figure 22. Comparison of the LSV spectra between the measurements with and without the presence of PRO (20 mg L^{-1}) based on the CN_900 membrane.

148
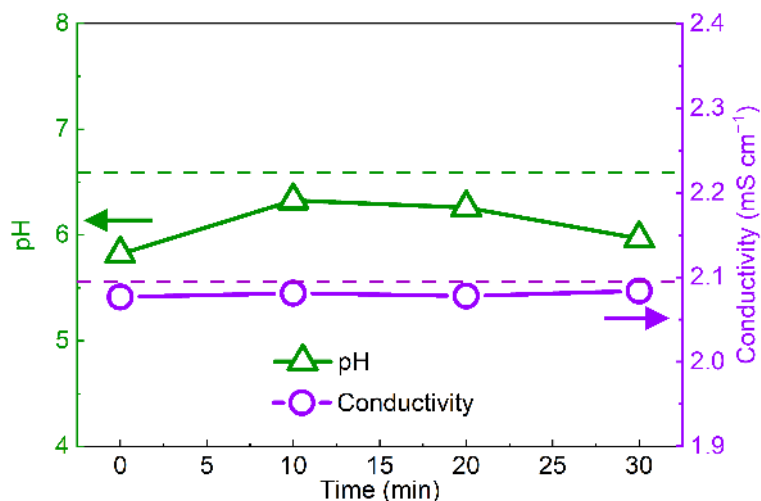
Supplementary Figure 23. Variations of the effluent pH and conductivity during the continuous EMF tests based on the CN_900 membrane and 20 mg L^{-1} PRO influent. The green and blue dotted lines indicate the influent pH and conductivity, respectively.

Supplementary Note 3.

Based on **Figure 6d** and **Figure 6g**, the kinetic degradation rate constants can be calculated for five different pollutants: 329.9 min^{-1} for RTD, 149.2 min^{-1} for CIP, 142.7 min^{-1} for CMT, 128.3 min^{-1} for SMX, and 114.1 min^{-1} for PRO. It can be seen that the reaction rate of direct anodic oxidation differs for different pollutants. RTD is more suitable for direct oxidation than the other four pollutants. The five pollutants (i.e., PRO, RTD, CIP, CMT, and SMX) used for the tests represent the most typical types of micropollutants of pharmaceuticals and personal care products that persist in water bodies: antibiotics (SMX and CIP), antagonists (CMT and RTD), and antihypertension (PRO). The reason we selected them is that they are difficult to degrade or remove by conventional water treatment technologies (e.g., biological processes, membrane bioreactors, etc.).

164
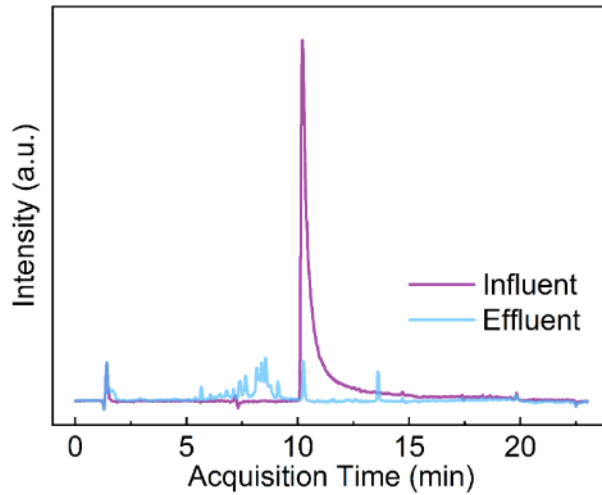
Supplementary Figure 24. Total ion current spectra measured by HPLC–MS/MS between the influent and effluent during the EMF tests based on the CN_900 membrane.

167

168
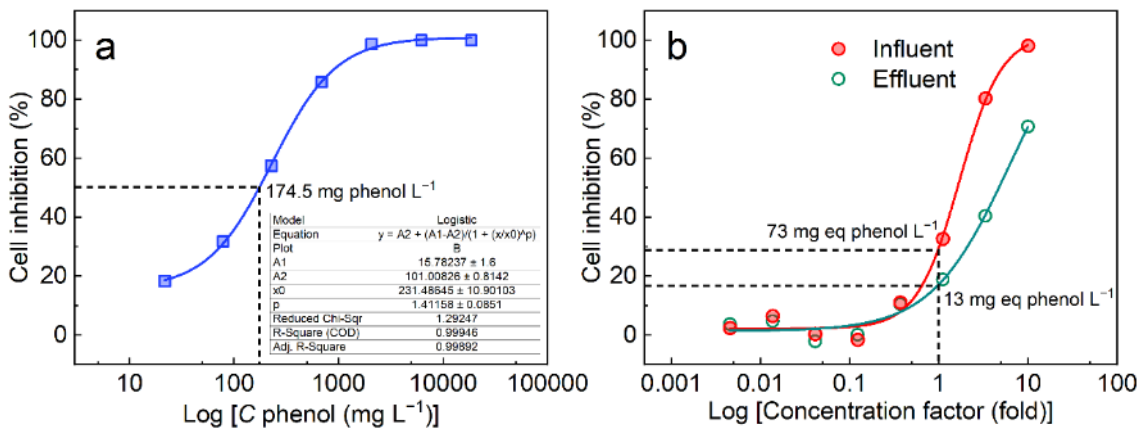
Supplementary Figure 25. (**a**) Standard curve of acute toxicity to *Vibrio fischeri* of phenol solution. The fitting parameters and EC50 values are shown in the figure. (**b**) Acute toxicity to *Vibrio fischeri* of the influent and effluent during the EMF tests based on the CN_900 membrane.
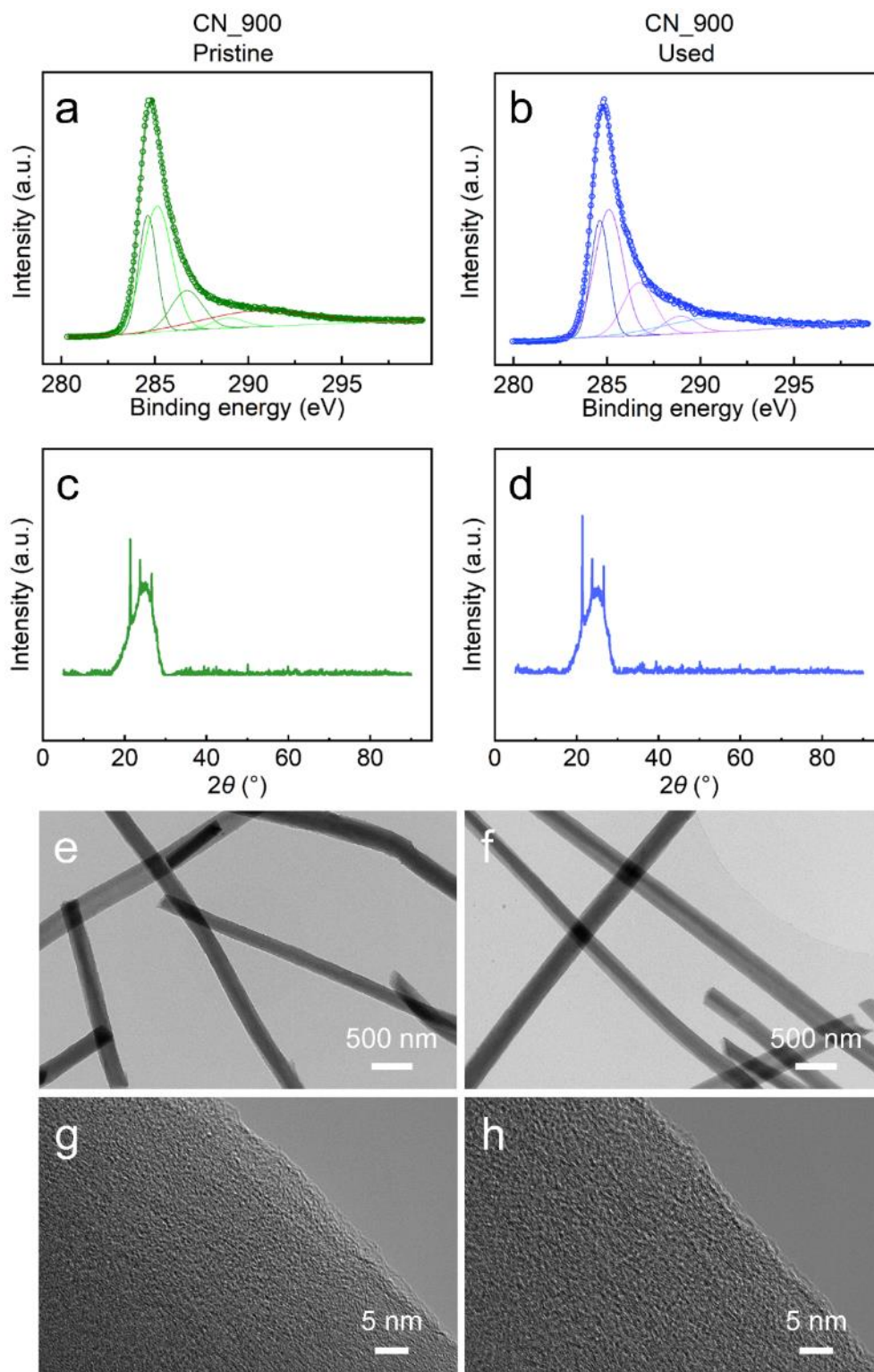
Supplementary Figure 26. Comparisons in terms of chemical compositions and morphology of the CN_900 between its pristine and long-term-used states. *C 1s* XPS spectra of the (**a**) pristine and (**b**) used CN_900. XRD spectra of the (**c**) pristine and (**d**) used CN_900. TEM images of the (**e**) pristine and (**f**) used CN_900. HRTEM images of the (**g**) pristine and (**h**) used CN_900.
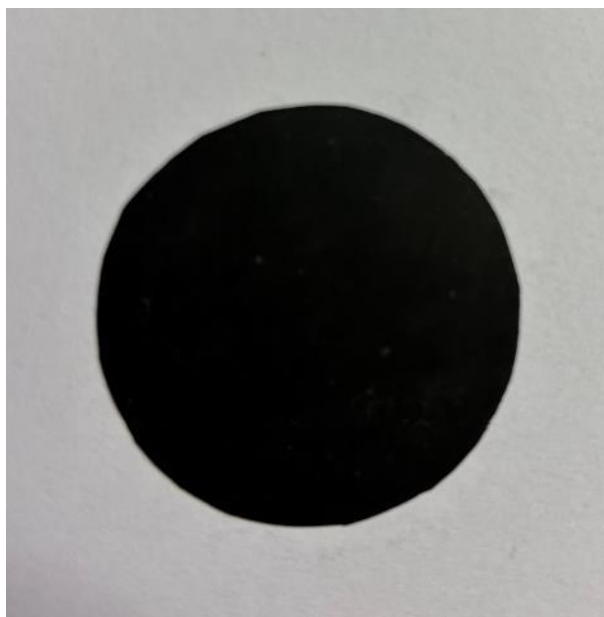
178

179 **Supplementary Figure 27.** Photograph of the CN_900 membrane after EMF process.

180
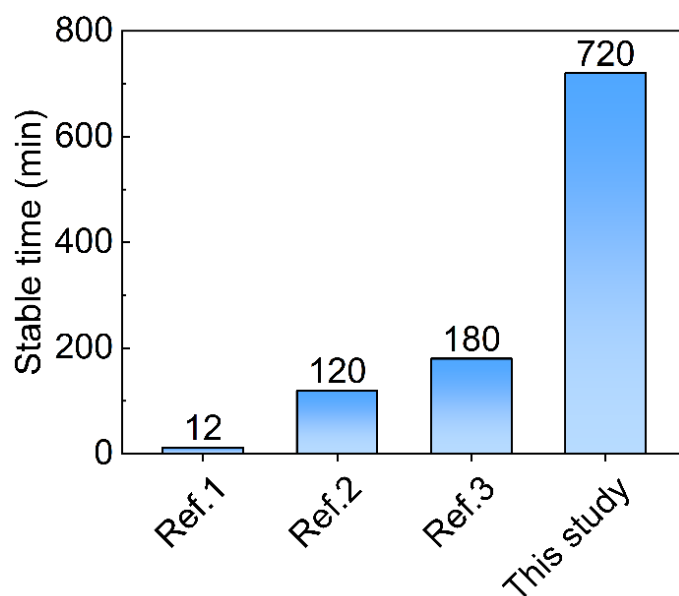
181

182 **Supplementary Figure 28.** Comparison of stable operation time between the CN_900

183 membrane in this study and other previously reported carbon-based electrocatalytic

184 membranes (more details in **Supplementary Table 2**).
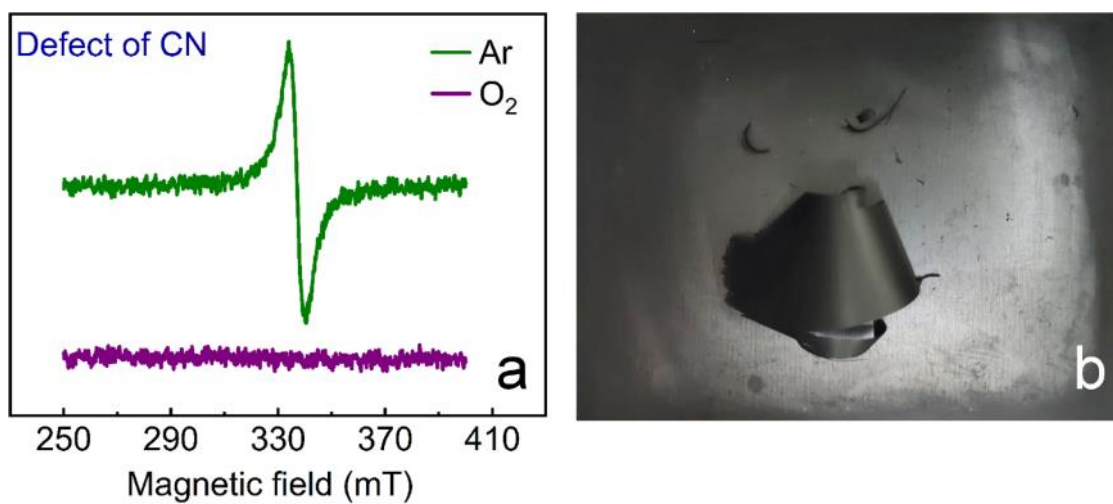
Supplementary Figure 29. (**a**) Comparison of ESR spectra of CN membranes carbonized at 900 °C under Ar and air atmospheres (with O_2). (**b**) Photographs of the CN membranes carbonized at 900 °C under air atmospheres (with O_2).

189　**Supplementary Table 1**. Calculated Hirshfeld charges, condensed Fukui functions and
190　condensed dual descriptors (CDD) of CN_900.

Atom	q(N)	q(N+1)	q(N−1)	f^-	f^+	f^0	CDD
1(C)	0.029	-0.0015	0.0521	0.023	0.0305	0.0268	0.0075
2(C)	0.019	-0.0033	0.0466	0.0276	0.0224	0.025	-0.0052
3(C)	-0.0062	-0.0093	0.0004	0.0066	0.0032	0.0049	-0.0034
4(C)	0.0083	-0.0211	0.0351	0.0268	0.0295	0.0281	0.0026
5(C)	-0.0018	-0.009	0.0026	0.0044	0.0072	0.0058	0.0027
6(C)	0.0047	0.0006	0.009	0.0043	0.0041	0.0042	-0.0002
7(C)	-0.0058	-0.0143	0.0041	0.0099	0.0086	0.0092	-0.0014
8(C)	0.021	-0.0023	0.0512	0.0302	0.0233	0.0267	-0.0069
9(N)	-0.1572	-0.1807	-0.1363	0.0209	0.0235	0.0222	0.0026
10(C)	0.0089	-0.0076	0.026	0.0171	0.0165	0.0168	-0.0006
11(C)	0.0074	-0.0058	0.0185	0.0111	0.0132	0.0121	0.0021
12(C)	-0.0054	-0.0146	0.0062	0.0117	0.0092	0.0104	-0.0025
13(C)	0.0048	0.0005	0.0098	0.0051	0.0042	0.0046	-0.0008
14(C)	-0.0027	-0.011	0.0032	0.0059	0.0083	0.0071	0.0025
15(C)	0.0133	-0.0114	0.0312	0.0179	0.0246	0.0213	0.0067
16(C)	0.0064	0.0002	0.0122	0.0059	0.0062	0.006	0.0003
17(C)	-0.0018	-0.0128	0.0038	0.0056	0.0109	0.0083	0.0053
18(C)	0.0243	0.0092	0.0401	0.0158	0.0152	0.0155	-0.0006
19(C)	-0.0086	-0.0214	0.0058	0.0145	0.0128	0.0136	-0.0017
20(C)	0.0155	-0.0038	0.0466	0.0311	0.0193	0.0252	-0.0117
21(N)	-0.1585	-0.1869	-0.1333	0.0252	0.0285	0.0268	0.0033
22(C)	-0.0398	-0.0546	-0.0199	0.0199	0.0148	0.0174	-0.0051
23(C)	0.0033	-0.0068	0.0153	0.0121	0.0101	0.0111	-0.002
24(C)	-0.0367	-0.0499	-0.019	0.0177	0.0132	0.0154	-0.0045
25(C)	-0.0032	-0.0149	0.0039	0.0072	0.0116	0.0094	0.0044

26(C)	0.0046	-0.0012	0.0111	0.0065	0.0058	0.0062	-0.0007
27(C)	-0.0086	-0.021	0.0063	0.0148	0.0124	0.0136	-0.0024
28(C)	0.021	0.0085	0.0399	0.0189	0.0124	0.0157	-0.0065
29(N)	-0.1546	-0.1825	-0.1288	0.0258	0.0279	0.0269	0.0022
30(C)	0.0315	0.0154	0.0412	0.0097	0.0161	0.0129	0.0064
31(C)	0.0205	0.0017	0.0445	0.024	0.0188	0.0214	-0.0053
32(C)	0.0053	0.001	0.0087	0.0033	0.0043	0.0038	0.001
33(C)	0.0056	0.003	0.0092	0.0036	0.0026	0.0031	-0.001
34(N)	-0.1595	-0.184	-0.1367	0.0228	0.0245	0.0237	0.0018
35(C)	0.0289	-0.0005	0.0464	0.0176	0.0294	0.0235	0.0119
36(C)	-0.0642	-0.1074	-0.013	0.0512	0.0432	0.0472	-0.008
37(C)	0.027	-0.0061	0.057	0.03	0.0331	0.0316	0.0031
38(C)	-0.068	-0.0976	-0.0367	0.0313	0.0296	0.0304	-0.0017
39(C)	-0.0377	-0.0441	-0.0306	0.0071	0.0064	0.0068	-0.0007
40(C)	0.0034	-0.0187	0.0265	0.0231	0.022	0.0226	-0.0011
41(C)	-0.0041	-0.0101	0.0006	0.0047	0.006	0.0054	0.0012
42(N)	-0.1601	-0.1785	-0.1417	0.0184	0.0184	0.0184	-0.0001
43(C)	-0.05	-0.0548	-0.0453	0.0048	0.0047	0.0048	0
44(C)	0.0106	0.002	0.021	0.0104	0.0085	0.0095	-0.0019
45(C)	-0.0066	-0.03	0.0146	0.0212	0.0233	0.0223	0.0021
46(C)	-0.0113	-0.0185	-0.0043	0.007	0.0072	0.0071	0.0002
47(N)	-0.1604	-0.1924	-0.1303	0.0301	0.032	0.031	0.002
48(C)	0.0309	0.0248	0.0344	0.0034	0.0061	0.0048	0.0026
49(H)	0.0443	0.0326	0.0543	0.01	0.0117	0.0109	0.0017
50(H)	0.0422	0.0334	0.0516	0.0094	0.0089	0.0091	-0.0005
51(H)	0.0444	0.0332	0.0558	0.0115	0.0111	0.0113	-0.0003
52(H)	0.0425	0.0353	0.0502	0.0077	0.0072	0.0075	-0.0004
53(H)	0.0472	0.0328	0.0634	0.0162	0.0143	0.0153	-0.0019

54(H)	0.0511	0.0381	0.0648	0.0137	0.013	0.0133	-0.0007
55(H)	0.0491	0.0368	0.0621	0.013	0.0123	0.0126	-0.0006
56(H)	0.0436	0.0353	0.0528	0.0092	0.0083	0.0087	-0.0008
57(H)	0.0452	0.0372	0.052	0.0068	0.0079	0.0074	0.0011
58(H)	0.0437	0.0343	0.0535	0.0098	0.0095	0.0096	-0.0003
59(H)	0.0422	0.0298	0.0518	0.0097	0.0123	0.011	0.0027
60(H)	0.046	0.0263	0.0653	0.0193	0.0197	0.0195	0.0003
61(H)	0.0435	0.0311	0.0566	0.0131	0.0124	0.0127	-0.0008
62(H)	0.0411	0.028	0.0533	0.0122	0.0131	0.0126	0.0009
63(H)	0.048	0.0319	0.0639	0.0159	0.016	0.016	0.0001
64(H)	0.0446	0.0371	0.0523	0.0076	0.0075	0.0076	-0.0001
65(H)	0.0414	0.0327	0.0503	0.0089	0.0087	0.0088	-0.0002
66(H)	0.0409	0.0329	0.0489	0.008	0.008	0.008	0
67(H)	0.0397	0.0321	0.0472	0.0075	0.0076	0.0076	0.0002
68(H)	0.0366	0.0289	0.0439	0.0073	0.0077	0.0075	0.0004
69(H)	0.0372	0.0254	0.0486	0.0114	0.0118	0.0116	0.0003
70(H)	0.0433	0.038	0.0481	0.0048	0.0053	0.0051	0.0005

191

Supplementary Table 2. Calculated Hirshfeld charges, condensed Fukui functions and CDD

of PRO.

Atom	q(N)	q(N+1)	q(N−1)	f⁻	f⁺	f⁰	CDD
1(O)	-0.231	-0.2387	-0.2218	0.0093	0.0077	0.0085	-0.0015
2(C)	0.0463	0.0412	0.0529	0.0066	0.0051	0.0059	-0.0014
3(C)	-0.0142	-0.0172	0.0021	0.0163	0.0031	0.0097	-0.0132
4(N)	-0.1681	-0.1648	-0.0653	0.1028	-0.0033	0.0497	-0.1061
5(C)	0.0176	0.0156	0.0297	0.0121	0.002	0.0071	-0.0101
6(C)	-0.0987	-0.1018	-0.0783	0.0204	0.0031	0.0117	-0.0173
7(C)	-0.0896	-0.0914	-0.0815	0.0082	0.0018	0.005	-0.0064
8(C)	0.029	0.0218	0.0342	0.0052	0.0072	0.0062	0.002
9(O)	-0.0763	-0.0986	-0.0491	0.0273	0.0222	0.0248	-0.005
10(C)	0.0748	0.0076	0.1127	0.0379	0.0671	0.0525	0.0292
11(C)	-0.0786	-0.1313	-0.0336	0.045	0.0528	0.0489	0.0078
12(C)	-0.0471	-0.1132	-0.0015	0.0456	0.0661	0.0558	0.0205
13(C)	-0.0549	-0.1269	0.0157	0.0705	0.0721	0.0713	0.0015
14(C)	-0.0024	-0.0204	0.009	0.0114	0.018	0.0147	0.0066
15(C)	-0.0402	-0.1284	0.0121	0.0523	0.0882	0.0702	0.0359
16(C)	-0.0428	-0.1098	-0.002	0.0409	0.067	0.0539	0.0261
17(C)	-0.044	-0.1102	0.0013	0.0453	0.0662	0.0557	0.0209
18(C)	-0.0383	-0.1278	0.0002	0.0385	0.0895	0.064	0.0511
19(C)	-0.0146	-0.0327	-0.0066	0.008	0.0181	0.013	0.0101
20(H)	0.1595	0.1547	0.1714	0.0119	0.0048	0.0084	-0.0071
21(H)	0.0264	0.0119	0.0463	0.0199	0.0144	0.0172	-0.0055
22(H)	0.0359	0.0223	0.0596	0.0237	0.0136	0.0186	-0.0101
23(H)	0.0158	0.0115	0.0419	0.0261	0.0043	0.0152	-0.0218
24(H)	0.0754	0.0838	0.0912	0.0158	-0.0084	0.0037	-0.0242
25(H)	0.0283	0.0166	0.0505	0.0222	0.0117	0.0169	-0.0105

26(H)	0.0256	0.0147	0.0515	0.0259	0.0109	0.0184	-0.0149
27(H)	0.0245	0.0194	0.0367	0.0121	0.0051	0.0086	-0.007
28(H)	0.0267	0.0324	0.0337	0.007	-0.0057	0.0006	-0.0127
29(H)	0.0278	0.0157	0.0478	0.02	0.0121	0.0161	-0.0079
30(H)	0.0308	0.0288	0.0411	0.0103	0.0019	0.0061	-0.0083
31(H)	0.0272	0.0358	0.0284	0.0012	-0.0086	-0.0037	-0.0099
32(H)	0.0342	0.0237	0.0453	0.0111	0.0106	0.0108	-0.0005
33(H)	0.0324	0.0219	0.0483	0.0159	0.0105	0.0132	-0.0054
34(H)	0.0373	0.0073	0.0595	0.0222	0.03	0.0261	0.0078
35(H)	0.0447	0.0053	0.0735	0.0288	0.0394	0.0341	0.0105
36(H)	0.04	0.0025	0.0711	0.031	0.0375	0.0343	0.0065
37(H)	0.0434	0.0012	0.0698	0.0263	0.0423	0.0343	0.0159
38(H)	0.0447	0.0039	0.0718	0.0271	0.0408	0.034	0.0137
39(H)	0.0459	0.0056	0.0715	0.0256	0.0403	0.0329	0.0147
40(H)	0.0467	0.0082	0.0592	0.0125	0.0385	0.0255	0.026

194

195 **Supplementary Table 3.** The referenced studies in the comparison of electrocatalysis

196 efficiency.

	Membrane materials	k, min^{-1}	1/EEO, m^3 order kWh^{-1}	Reference
	N-doped defective carbon nanofiber	114.1	34.48	This study
S1	BDD/ADE–Pt/CF	0.0029	0.015	[5]
S2	Nb/BDD	0.0101	0.024	[6]
S3	Ti/Ir$_x$Ta$_y$O$_2$/[Bi$_2$O$_3$]$_z$[TiO$_2$]$_{1-z}$	0.0217	0.208	[7]
S4	Ti/Pt	0.0326	0.227	[8]
S5	Ti-Pt	0.0226	0.571	[9]
S6	Pt	0.9210	3.030	[10]
S7	Pd–Pt–ceramic membrane	4.6072	57.67	[11]
S8	Cobalt-doped Black-TiO$_2$ nanotube array	0.0048	0.011	[12]
S9	Ti/Ru$_{0.3}$Ti$_{0.7}$O	0.0161	0.016	[13]
S10	Electrodeposited polytetrafluoroethylene (PTFE)-doped β-PbO$_2$	0.0154	0.020	[14]
S11	3G/SnO$_2$/CFs	0.238	0.024	[15]
S12	A composite wire mesh anode (composed of blue TiO$_2$ nanotubes covered with SnO$_2$–Sb$_2$O$_3$)	0.0076	0.121	[16]
S13	TiO$_2$ nanotubes arrays electrode	0.0253	0.122	[17]
S14	Sb-doped SnO$_2$ with TiO$_2$ nanotube clusters on Ti mesh	0.0676	0.312	[18]
S15	Ti/SnO$_2$-Sb	0.24	0.690	[19]
S16	TiO$_2$@SnO$_2$–Sb	0.0019	0.805	[20]
S17	Ti/SnO$_2$-Sb/Ce-PbO$_2$	0.649	1.344	[21]
S18	Blue-TiO$_2$ nanotubes	0.0071	1.587	[22]
S19	Macroporous-Ti-enhanced TiO$_2$ nanotube	0.124	1.724	[23]

array/SnO$_2$-Sb$_2$O$_3$

S20	Bi-doped SnO$_2$–Ti$_n$O$_{2n-1}$	115.1	2.381	[24]
S21	SnO$_2$-Sb reactive anodic filter	1.485	3.030	[25]
S22	Ti$_4$O$_7$	20.98	3.704	[26]
S23	Blue-colored TiO$_2$ nanotube arrays	0.403	11.63	[27]
S24	Ti$_4$O$_7$ reactive electrochemical membrane	0.0298	4.303	[28]
S25	Porous Ti-ENTA/SnO$_2$-Sb anode	0.1197	0.049	[29]
S26	Flow-through Ti/TiO$_2$-NTA/Ti$_4$O$_7$ anode	0.083	0.758	[30]
S27	TiSO electroactive ceramic membrane	0.124	0.235	[31]
S28	Reduced TiO$_2$ nanotube arrays-based Ti membrane	0.0395	1.818	[32]
S29	Porous Ti–ENTA/SnO$_2$–Sb	0.0914	1.613	[33]
S30	IrO$_2$ and Ta$_2$O$_5$ coating on titanium mesh and Fe foam coated with Pd	0.0894	0.019	[34]
S31	Blue TiO$_2$ nanotube electrocatalytic membrane	0.235	3.704	[35]
S32	Multi-walled carbon nanotube	2.1	0.500	[36]
S33	Carbon nanotube electrochemical filter	98.9	6.933	[37]
S34	Coal-based carbon membrane	3.985	20.31	[38]
S35	FeNi LDH/CNT membranes	0.0328	2.580	[39]
S36	Graphene sponge	1.002	0.149	[40]
S37	FeOCl-CNT filters	106.0	6.848	[41]
S38	CNT filter modified with MIL-101(Fe)	0.015	7.297	[42]
S39	BDD	0.0388	0.005	[43]
S40	BDD	0.0158	0.040	[44]
S41	BDD	0.0715	1.429	[45]

197

Supplementary Table 4. The referenced studies in the comparison of stable operation time in **Supplementary Figure 28**.

Reference	Electrocatalyst	Stable time, min	Target pollutant
[46]	Hybrid graphene-decorated metal hollow fiber membrane	12	Paracetamol
[36]	Multi-walled carbon nanotube filter	120	Sulfamethoxazole
[37]	Carbon nanotube electrochemical filter	180	Tetracycline
This study	N-doped defective carbon nanofiber membrane	720	Propranolol

Supplementary Table 5. The boundary condition and related coefficients used in the multiphysics simulations.

Parameter	Value	Definition
μ_in	3×10^{-4} m s^{-1}	flow-in velocity
n	1	number of electrons transferred
a	0.5	electron transfer coefficient
E^0	2.5 V	formal potential
E	3 V	applied potential
i_0	8×10^{-4} A m^{-2}	exchange current density
C_0	0.0676 mol m^{-3}	pollutant concentration at inlet
κ_s	0.22 S m^{-1}	conductivity of solution
D	5×10^{-10} m^2 s^{-1}	pollutant diffusivity
T	293.15 K	room temperature

References

1. Melis N, Mocci F, Vacca A & Pilia L. Novel homogeneous selective electrocatalysts for CO_2 reduction: an electrochemical and computational study of cyclopentadienyl-phenylendiamino-cobalt complexes. *Sustainable Energy Fuels* **4**, 5609–5617 (2020).

209 2.   Duan X, *et al.* Electrocatalytic degradation of 2,4-dichlorophenol by a 3DG-PbO$_2$
210   powdered anode: Experimental and theoretical insights. *Sep Purif Technol* **282**, 120003
211   (2022).
212 3.   Lu T & Chen F. Multiwfn: A multifunctional wavefunction analyzer. *J Comput Chem*
213   **33**, 580–592 (2012).
214 4.   Lu T & Chen Q. Realization of conceptual density functional theory and information-
215   theoretic approach in Multiwfn program. In: *Conceptual Density Functional Theory*)
216   (2022).
217 5.   Isarain-Chávez E, *et al.* Degradation of pharmaceutical beta-blockers by
218   electrochemical advanced oxidation processes using a flow plant with a solar compound
219   parabolic collector. *Water Res* **45**, 4119–4130 (2011).
220 6.   García-Espinoza JD, Zolfaghari M & Mijaylova Nacheva P. Synergistic effect between
221   ultraviolet irradiation and electrochemical oxidation for removal of humic acids and
222   pharmaceuticals. *Water Environ J* **34**, 232–246 (2020).
223 7.   Jasper JT, Shafaat OS & Hoffmann MR. Electrochemical transformation of trace
224   organic contaminants in latrine wastewater. *Environ Sci Technol* **50**, 10198–10208
225   (2016).
226 8.   Song H, *et al.* Nonradical oxidation from electrochemical activation of peroxydisulfate
227   at Ti/Pt anode: Efficiency, mechanism and influencing factors. *Water Res* **116**, 182–193
228   (2017).
229 9.   Zambrano J & Min B. Comparison on efficiency of electrochemical phenol oxidation
230   in two different supporting electrolytes (NaCl and Na$_2$SO$_4$) using Pt/Ti electrode.
231   *Environ Technol Innovation* **15**, 100382 (2019).
232 10. Mbaye M, *et al.* Rapid removal of fungicide thiram in aqueous medium by electro-
233   Fenton process with Pt and BDD anodes. *Sep Purif Technol* **281**, 119837 (2022).
234 11. Zhao Y, *et al.* Janus electrocatalytic flow-through membrane enables highly selective
235   singlet oxygen production. *Nat Commun* **11**, 6228 (2020).
236 12. Yang Y, *et al.* Cobalt-doped black TiO$_2$ nanotube array as a stable anode for oxygen
237   evolution and electrochemical wastewater treatment. *ACS Catal* **8**, 4278–4287 (2018).
238 13. Fukunaga MT, Guimarães JR & Bertazzoli R. Kinetics of the oxidation of
239   formaldehyde in a flow electrochemical reactor with TiO$_2$/RuO$_2$ anode. *Chem Eng J*
240   **136**, 236–241 (2008).
241 14. Sánchez-Montes I, *et al.* Evolution of the antibacterial activity and oxidation
242   intermediates during the electrochemical degradation of norfloxacin in a flow cell with
243   a PTFE-doped β-PbO$_2$ anode: Critical comparison to a BDD anode. *Electrochim Acta*
244   **284**, 260–270 (2018).
245 15. Yu S, *et al.* Electrospun PAN-based graphene/SnO$_2$ carbon nanofibers as anodic
246   electrocatalysis microfiltration membrane for sulfamethoxazole degradation. *J Membr*
247   *Sci* **614**, 118368 (2020).
248 16. Meng X, *et al.* Development of a three-dimensional electrochemical system using a
249   blue TiO$_2$/SnO$_2$–Sb$_2$O$_3$ anode for treating low-ionic-strength wastewater. *Environ Sci*
250   *Technol* **53**, 13784–13793 (2019).

251 17. Wang K, *et al.* Insights into electrochemical decomposition mechanism of
252 lipopolysaccharide using TiO_2 nanotubes arrays electrode. *J Hazard Mater* **391**, 122259
253 (2020).

254 18. Huang L, *et al.* Construction of TiO_2 nanotube clusters on Ti mesh for immobilizing
255 $Sb-SnO_2$ to boost electrocatalytic phenol degradation. *J Hazard Mater* **393**, 122329
256 (2020).

257 19. Zhou C, Wang Y, Chen J & Niu J. Porous Ti/SnO_2-Sb anode as reactive electrochemical
258 membrane for removing trace antiretroviral drug stavudine from wastewater. *Environ*
259 *Int* **133**, 105157 (2019).

260 20. Zheng J, Wang Z, Ma J, Xu S & Wu Z. Development of an electrochemical ceramic
261 membrane filtration system for efficient contaminant removal from waters. *Environ Sci*
262 *Technol* **52**, 4117–4126 (2018).

263 21. Xu L, Ma X, Niu J, Chen J & Zhou C. Removal of trace naproxen from aqueous solution
264 using a laboratory-scale reactive flow-through membrane electrode. *J Hazard Mater*
265 **379**, 120692 (2019).

266 22. Cai J, Zhou M, Pan Y, Du X & Lu X. Extremely efficient electrochemical degradation
267 of organic pollutants with co-generation of hydroxyl and sulfate radicals on Blue-TiO_2
268 nanotubes anode. *Appl Catal B* **257**, 117902 (2019).

269 23. Chen M, *et al.* Development of a highly efficient electrochemical flow-through anode
270 based on inner in-site enhanced TiO_2-nanotubes array. *Environ Int* **140**, 105813 (2020).

271 24. Gayen P, Chen C, Abiade JT & Chaplin BP. Electrochemical oxidation of atrazine and
272 clothianidin on Bi-doped SnO_2–Ti_nO_{2n-1} electrocatalytic reactive electrochemical
273 membranes. *Environ Sci Technol* **52**, 12675–12684 (2018).

274 25. Yang C, Fan Y, Shang S, Li P & Li X-y. Fabrication of a permeable SnO_2-Sb reactive
275 anodic filter for high-efficiency electrochemical oxidation of antibiotics in wastewater.
276 *Environ Int* **157**, 106827 (2021).

277 26. Misal SN, Lin M-H, Mehraeen S & Chaplin BP. Modeling electrochemical oxidation
278 and reduction of sulfamethoxazole using electrocatalytic reactive electrochemical
279 membranes. *J Hazard Mater*, 121420 (2019).

280 27. Xu L, *et al.* Effective degradation of aqueous carbamazepine on a novel blue-colored
281 TiO_2 nanotube arrays membrane filter anode. *J Hazard Mater* **402**, 123530 (2021).

282 28. Zhi D, *et al.* Development of ozonation and reactive electrochemical membrane
283 coupled process: Enhanced tetracycline mineralization and toxicity reduction. *Chem*
284 *Eng J* **383**, 123149 (2020).

285 29. Hakizimana I, *et al.* Effective degradation of amoxicillin by multi-stage flow-through
286 electrochemical system using porous electrodes. *Sep Purif Technol* **300**, 121832 (2022).

287 30. Meng C, *et al.* Efficient electrochemical oxidation of COVID-19 treatment drugs
288 favipiravir by a novel flow-through Ti/TiO_2-NTA/Ti_4O_7 anode. *Electrochim Acta* **430**,
289 141055 (2022).

290 31. Wang S, Pei S, Zhang J, Huang J & You S. Flow-through electrochemical removal of
291 benzotriazole by electroactive ceramic membrane. *Water Res* **218**, 118454 (2022).

292 32. Zeng W, *et al.* Efficient electrochemical oxidation of sulfamethoxazole by a novel

293   reduced TiO$_2$ nanotube arrays-based flow-through electrocatalytic membrane. *Sep*
294   *Purif Technol* **289**, 120720 (2022).

295 33.   Zhang C, Zhao X, Wang C & Pan S. Novel multistage electrochemical flow-through
296   mode (EFTM) with porous electrodes for reclaimed wastewater treatment in pipes. *ACS*
297   *ES&T Water* **1**, 653–660 (2021).

298 34.   Hyldegaard BH, Ottosen LM & Alshawabkeh AN. Transformation of
299   tetrachloroethylene in a flow-through electrochemical reactor. *Sci Total Environ* **707**,
300   135566 (2020).

301 35.   Wang L*, et al.* Blue TiO$_2$ nanotube electrocatalytic membrane electrode for efficient
302   electrochemical degradation of organic pollutants. *Chemosphere* **306**, 135628 (2022).

303 36.   Tan T-Y*, et al.* Electrochemically enhanced simultaneous degradation of
304   sulfamethoxazole, ciprofloxacin and amoxicillin from aqueous solution by multi-
305   walled carbon nanotube filter. *Sep Purif Technol* **235**, 116167 (2020).

306 37.   Liu Y*, et al.* Degradation of the common aqueous antibiotic tetracycline using a carbon
307   nanotube electrochemical filter. *Environ Sci Technol* **49**, 7974–7980 (2015).

308 38.   Pan Z*, et al.* Electrochemical microfiltration treatment of bisphenol A wastewater using
309   coal-based carbon membrane. *Sep Purif Technol* **227**, 115695 (2019).

310 39.   Yang L, Xu D, Yang H, Luo X & Liang H. Structurally-controlled FeNi LDH/CNTs
311   electro-Fenton membrane for in-situ electro-generation and activation of hydroxyl
312   radicals toward organic micropollutant treatment. *Chem Eng J* **432**, 134436 (2022).

313 40.   Ormeno-Cano N & Radjenovic J. Electrochemical degradation of antibiotics using
314   flow-through graphene sponge electrodes. *J Hazard Mater* **431**, 128462 (2022).

315 41.   Li Z*, et al.* Carbon nanotube filter functionalized with iron oxychloride for flow-
316   through electro-Fenton. *Appl Catal B* **260**, 118204 (2020).

317 42.   Dai Y*, et al.* Carbon nanotube filter functionalized with MIL-101(Fe) for enhanced
318   flow-through electro-Fenton. *Environ Res* **204**, 112117 (2022).

319 43.   Carneiro JF*, et al.* The effect of the supporting electrolyte on the electrooxidation of
320   enrofloxacin using a flow cell with a BDD anode: Kinetics and follow-up of oxidation
321   intermediates and antimicrobial activity. *Chemosphere* **206**, 674–681 (2018).

322 44.   Coledam DAC, Aquino JM, Silva BF, Silva AJ & Rocha-Filho RC. Electrochemical
323   mineralization of norfloxacin using distinct boron-doped diamond anodes in a filter-
324   press reactor, with investigations of toxicity and oxidation by-products. *Electrochim*
325   *Acta* **213**, 856–864 (2016).

326 45.   Carneiro JF, Aquino JM, Silva BF, Silva AJ & Rocha-Filho RC. Comparing the
327   electrochemical degradation of the fluoroquinolone antibiotics norfloxacin and
328   ciprofloxacin using distinct electrolytes and a BDD anode: evolution of main oxidation
329   byproducts and toxicity. *J Environ Chem Eng* **8**, 104433 (2020).

330 46.   Huong Le TX*, et al.* Hybrid graphene-decorated metal hollow fibre membrane reactors
331   for efficient electro-Fenton - Filtration co-processes. *J Membr Sci* **587**, 117182 (2019).